# Impact of Proppant Pumping Schedule on Well Production for Slickwater Fracturing

**Shaowen Mao, Prashanth Siddhamshetty,** and **Zhuo Zhang,** Texas A&M University; **Wei Yu,** University of Texas at Austin; and **Troy Chun, Joseph Sang-Il Kwon,** and **Kan Wu,** Texas A&M University

## Summary

Slickwater fracturing has become one of the most leveraging completion technologies in unlocking hydrocarbon in unconventional reservoirs. In slickwater treatments, proppant transport becomes a big concern because of the inefficiency of low-viscosity fluids to suspend the particles. Many studies have been devoted to proppant transport experimentally and numerically. However, only a few focused on the proppant pumping schedules in slickwater fracturing. The impact of proppant schedules on well production remains unclear. The goal of our work is to simulate the proppant transport under real pumping schedules (multisize proppants and varying concentration) at the field scale and quantitatively evaluate the effects of proppant schedules on well production for slickwater fracturing.

The workflow consists of three steps. First, a validated 3D multiphase particle-in-cell (MP-PIC) model has been used to simulate the proppant transport at real pumping schedules in a field-scale fracture (180-m length, 30-m height). Second, we applied a propped fracture conductivity model to calculate the distribution of propped fracture width, permeability, and fracture conductivity. In the last step, we incorporated the fracture geometry, propped fracture conductivity, and the estimated unpropped fracture conductivity into a reservoir simulation model to predict gas production.

Based on the field designs of pumping schedules in slickwater treatments, we have generated four proppant schedules, in which 100-mesh and 40/70-mesh proppants were loaded successively with stair-stepped and incremental stages. The first three were used to study the effects of the mass percentages of the multisize proppants. From Schedules 1 through 3, the mass percentage of 100-mesh proppants is 30, 50, and 70%, respectively. Schedule 4 has the same proppant percentage as Schedule 2 but has a flush stage after slurry injection. The comparison between Schedules 2 and 4 enables us to evaluate the effect of the flush stage on well production.

The results indicate that the proppant schedule has a significant influence on treatment performance. The schedule with a higher percentage of 100-mesh proppants has a longer proppant transport distance, a larger propped fracture area, but a lower propped fracture conductivity. Then, the reservoir simulation results show that both the small and large percentages of 100-mesh proppants cannot maximize well production because of the corresponding small propped area and low propped fracture conductivity. Schedule 2, with a median percentage (50%) of 100-mesh proppants, has the highest 1,000-day cumulative gas production. For Schedule 4, the flush stage significantly benefits the gas production by 8.2% because of a longer and more uniform proppant bed along the fracture.

In this paper, for the first time, we provide both the qualitative explanation and quantitative evaluation for the impact of proppant pumping schedules on the performance of slickwater treatments at the field scale by using an integrated numerical simulation workflow, providing crucial insights for the design of proppant schedules in the field slickwater treatments.

## Introduction

Slickwater fracturing has become a dominant technology in obtaining commercial production from unconventional reservoirs (Schein 2005; Tang et al. 2018, 2019; Li et al. 2020). In slickwater treatments, proppant transport is a challenging issue because of the limited carrying capacity of the low-viscosity fluids (Palisch et al. 2010). Many researchers have conducted studies on the proppant transport in slickwater fracturing both experimentally (Kern et al. 1959; Babcock et al. 1967; Tong and Mohanty 2016; Alotaibi and Miskimins 2018; Chun et al. 2019; Miskimins and Alotaibi 2019) and numerically (Sharma and Gadde 2005; Tsai et al. 2013; Kong et al. 2015; Zeng et al. 2016, 2019; Hu et al. 2018; Kou et al. 2018; Mao et al. 2019; Zhang et al. 2020). Most of them focused on particle transport behaviors (suspension and settling), the influence of slurry properties, and the effects of complex fracture geometries. One frequently overlooked aspect of the proppant transport in slickwater fracturing is the impact of proppant pumping schedules.

Scheduling the proppant addition is critical during the treatment, of which the primary goal is to create specified fracture properties and prevent an undesired screenout (Economides and Nolte 1989). Since the 1980s, a few studies have been devoted to the design of a proppant schedule (Crawford 1983; Nolte 1986; Meng and Brown 1987; Gu and Desroches 2003; Dontsov and Peirce 2014; Siddhamshetty et al. 2018, 2019). Nolte (1986) proposed an analytical formula to generate a schedule based on fluid efficiency (the ratio of fracture volume to injected fluid volume). Nolte's method is commonly used in the industry because of its ease of use. Gu and Desroches (2003) developed a more accurate pumping schedule generator based on a pseudo-3D fracture model. However, the iterative algorithm employed to solve an inverse problem makes this method computationally expensive. To balance the accuracy and computational cost, Dontsov and Peirce (2014) presented another model-based pumping schedule generator by neglecting the effect of proppant on fracture propagation. All these methods assume negligible proppant gravitational settling and uniform proppant distribution in the fractures, which is inappropriate for the schedule design in slickwater fracturing.

To better consider the proppant transport behaviors, Hu et al. (2018) applied the dense discrete phase method (DDPM) to study the effects of proppant schedules in slickwater treatments. However, this study was limited to the lab scale because of the extensive computational cost. Besides, the authors only compared the proppant distribution under different schedules during the pumping process and did not consider how the proppant distribution would affect the well production. To our best knowledge, no studies have focused on the quantitative evaluation and optimization of the proppant schedules in slickwater treatments.

The difficulty of designing and optimizing proppant schedules in slickwater treatments lies in the scarcity of suitable proppant transport models (Handren and Palisch 2009). Current proppant transport models are within two frameworks: Eulerian-Eulerian (E-E) framework and Eulerian-Lagrangian (E-L) framework.



This paper (SPE 204235) was revised for publication from paper URTEC-2020-2630-MS, presented at the SPE/AAPG/SEG Unconventional Resources Technology Conference, Virtual, 20–22 July 2020. Original manuscript received for review 1 June 2020. Revised manuscript received for review 8 September 2020. Paper peer approved 28 September 2020.

The E-E framework treats both the fluid and the particle as a continuum and has an advantage of computational efficiency. E-E methods, including the concentration model (Sharma and Gadde 2005; Liu 2006; Gu and Mohanty 2014; Dontsov and Peirce 2015; Roostaei et al. 2018) and two-fluid models (Mobbs and Hammond 2001; Boronin and Osiptsov 2014), are widely used in commercial software and suitable for conventional high-viscosity fluid treatments. However, it is challenging for them to handle complex proppant transport mechanisms in slickwater fracturing, such as particle-particle interaction, particle washout, and multisize proppants.

Treating the fluid as a continuum while the particles are in discrete phases, the E-L framework can capture more physical mechanisms. One of the most common E-L methods for proppant simulation is the computational fluid dynamics-discrete element method (CFD-DEM). Many researchers have employed this method to simulate the proppant transport in the wellbore (Wu et al. 2017; Yi et al. 2018) and different fracture geometries (Zeng et al. 2016; Kou et al. 2018, 2019; Zhang et al. 2019). The DDPM is also within the E-L framework and used by some researchers (Tong and Mohanty 2016; Hu et al. 2018; Almulhim et al. 2020). Both the CFD-DEM and DDPM can present accurate results in proppant simulation. Nevertheless, they are extremely computationally demanding and not suitable for field-scale problems.

To address field-scale problems and capture the important physics of the proppant transport in slickwater treatments, in this study we have employed an efficient MP-PIC method to simulate proppant transport under different schedules. The MP-PIC method is also within the E-L framework, but it is much more efficient than CFD-DEM and DDPM. Several researchers (Patankar and Joseph 2001; Tsai et al. 2013; Mao et al. 2019; Zeng et al. 2019; Zhang et al. 2020) have applied the method to simulate proppant transport in different fracture geometries and performed simple parametric studies. Instead of considering individual particles, the MP-PIC method treats several particles as a computational parcel, which significantly saves the calculation time and enables us to perform the field-scale proppant simulation. The accuracy and efficiency of the MP-PIC method in proppant simulation were validated by indoor experiments (Mao et al. 2020; Zhang et al. 2020).

Benefitting from the MP-PIC method, we can simulate the proppant transport under real pumping schedules with varying concentrations and multiple proppant sizes (40/70 and 100 mesh). Four pumping schedules were designed based on the typical schedules in the field slickwater treatments to investigate the effects of the mass percentages of multisize proppants and the impact of a flush stage. Apart from the proppant simulation, we also estimated the propped fracture conductivity and compared gas production. Combining the field-scale proppant simulation, propped fracture conductivity calculation, and reservoir simulation, this work presents an integrated workflow to quantify the effects of real proppant schedules on well production. The results can provide us with some insights into the design and optimization of proppant schedules in slickwater fracturing.

## Methodology

The workflow investigating the impact of proppant pumping schedules on well production consists of three steps: proppant simulation, propped fracture conductivity calculation, and gas production simulation **(Fig. 1).** In the first step, the MP-PIC method has been employed to simulate the proppant distribution under four real pumping schedules. Based on the proppant simulation results, we developed a propped fracture conductivity model to calculate the distribution of propped width, permeability, and fracture conductivity after fracturing treatments. Finally, we incorporated the propped fracture geometry and fracture conductivity into a reservoir simulation model to compare the gas production.

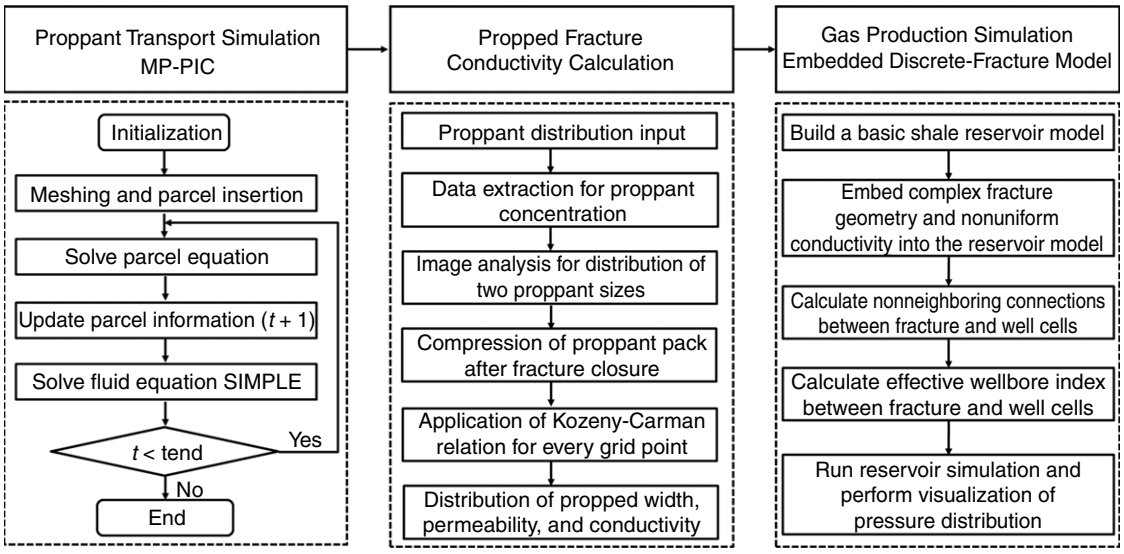

**Fig. 1—Integrated flow chart for investigating the impact of proppant pumping schedules on well production. The flow chart consists of three steps: (1) proppant transport simulation, (2) propped fracture conductivity calculation; and (3) gas production simulation.**

**Proppant Transport Simulation.** The MP-PIC method for proppant transport simulation is one of the E-L methods, treating the fluid as a continuum phase while particles as discrete phases. This method can accurately simulate complex field-scale proppant transport processes and has been validated by the indoor experiments (Mao et al. 2020; Zhang et al. 2020). The governing equations are presented below.

***Fluid Phase.*** The fluid phase is described by the continuity equation (with no interphase mass transfer) and the momentum equation.

$$\frac{\partial\left(\alpha_f \rho_f\right)}{\partial t} + \nabla \cdot \left(\alpha_f \rho_f \boldsymbol{u}_f\right) = 0, \quad (1)$$

where $\alpha_f$ is the fluid volume fraction; $\boldsymbol{u}_f$ is the fluid velocity, m/s; and $\rho_f$ is the fluid density, kg/m$^3$.

$$\frac{\partial(\alpha_f\rho_f\boldsymbol{u}_f)}{\partial t}+\nabla\cdot(\alpha_f\rho_f\boldsymbol{u}_f\boldsymbol{u}_f)=-\nabla p-\boldsymbol{F}_{fp}+\alpha_f\rho_f\boldsymbol{g}+\nabla\cdot\alpha_f\boldsymbol{\tau}_f, \quad \ldots\ldots (2)$$

where $\rho_f$ is the fluid density; $p$ is the fluid pressure, Pa; $g$ is the gravitational acceleration, m/s$^2$; $\boldsymbol{F}_{fp}$ is the rate of momentum change per volume between the fluid and particulate phases, Pa; and $\boldsymbol{\tau}_f$ is the fluid stress tensor, Pa. For Newtonian fluids, the stress can be represented as

$$\tau_{ij}=2\mu_f S_{ij}-\frac{2}{3}\mu_f\delta_{ij}\frac{\partial u_i}{\partial x_j}, \quad \ldots\ldots (3)$$

$$S_{ij}=\frac{1}{2}\left(\frac{\partial u_i}{\partial x_j}+\frac{\partial u_j}{\partial x_i}\right), \quad \ldots\ldots (4)$$

where $\mu_f$ is fluid viscosity, Pa·s; and $S_{ij}$ is the nonhydrostatic part of the stress tensor, Pa.

***Particulate Phase.*** For particulate phases, instead of addressing individual particles, we treat the particles as computational parcels in both physical and velocity spaces. Every parcel consists of several particles that have identical density, volume, velocity, and location. The particle motion is governed by Newton's second law.

$$\boldsymbol{A}=\frac{d\boldsymbol{u}_p}{dt}=D_p(\boldsymbol{u}_f-\boldsymbol{u}_p)-\frac{1}{\rho_p}\nabla p+\boldsymbol{g}-\frac{1}{\alpha_p\rho_p}\nabla\boldsymbol{\tau}_p+\frac{(\langle\boldsymbol{u}_p\rangle-\boldsymbol{u}_p)}{2\tau_D}, \quad \ldots\ldots (5)$$

where $\rho_p$ is the particle density, kg/m$^3$; $\alpha_p$ is the particle volume fraction; $\boldsymbol{\tau}_p$ represents the particle normal stress, Pa; and $\langle\boldsymbol{u}_p\rangle$ is the mass averaged velocity of the surrounding particles, m/s. The five terms on the right-hand side of Eq. 5 represents the effect of fluid-particle drag, dynamic pressure gradient, gravity acceleration, interparticle stress, and collision damping (O'Rourke and Snider 2010), respectively. The drag force model proposed by Wen and Yu (1966) is used to calculate the drag coefficient, s$^{-1}$.

$$D_p=C_d\frac{3}{8}\frac{\rho_f}{\rho_p}\frac{|\boldsymbol{u}_f-\boldsymbol{u}_p|}{R_p}, \quad \ldots\ldots (6)$$

$$C_d=\begin{cases}\dfrac{24}{\mathrm{Re}}\left(\alpha_f^{-2.65}+\dfrac{\mathrm{Re}^{\frac{2}{3}}}{6}\alpha_f^{-1.78}\right), \mathrm{Re}<1000\\ 0.44\alpha_f^{-2.65}, \mathrm{Re}>1000,\end{cases} \quad \ldots\ldots (7)$$

$$\mathrm{Re}=\frac{2\rho_f|\boldsymbol{u}_f-\boldsymbol{u}_p|r_p}{\mu_f}, \quad \ldots\ldots (8)$$

$$r_p=\left(\frac{3V_p}{4\pi}\right)^{\frac{1}{3}}, \quad \ldots\ldots (9)$$

where $C_d$ is the dimensionless drag coefficient; Re is the particle Reynolds number; $r_p$ is the particle radius, m; and $V_p$ is the particle volume, m$^3$, assuming spherical particles.

The particle stress model proposed by Harris and Crighton (1994) is employed to calculate the isotropic interparticle stress. The particle stress term can prevent particles from exceedingly packing.

$$\tau_p=\frac{P_s\alpha_p^{\beta}}{\max[\alpha_{cp}-\alpha_p,\zeta(1-\alpha_p)]}, \quad \ldots\ldots (10)$$

where $\alpha_{cp}$ is the close-packing particle volume fraction, and both $P_s$ and $\beta$ are constants (Auzerais et al. 1988). In the denominator, a smaller number $\zeta$ (with order of $10^{-7}$) is used to avoid the singularity (Snider 2001).

For the collision damping term on the right-hand side of Eq. 5, $\langle\boldsymbol{u}_p\rangle$ is the mass averaged velocity of the particle phase, m/s; $\tau_D$ is the relaxation time, seconds (O'Rourke and Snider 2010). It addresses the effect of particle collision on damping fluctuating particle velocities.

***Coupling Issues.*** The MP-PIC method couples the fluid phase and particle phase through interphase momentum transfer, which consists of the fluid/particle drag force and dynamic pressure gradient.

$$\boldsymbol{F}_{fp}=\iiint\phi V_p\rho_p\left[D_p(\boldsymbol{u}_f-\boldsymbol{u}_p)-\frac{1}{\rho_p}\nabla p\right]dV_p d\rho_p du_p. \quad \ldots\ldots (11)$$

***Numerical Procedures.*** Fig. 1 presents the whole numerical procedure for the MP-PIC method, in which the fluid phase is discretized by the finite volume method in Eulerian grids, and the particles are tracked as Lagrangian points. Therefore, an interpolation function is required to exchange information between the Eulerian grids and particle positions. Because the study uses a staggered grid where momentum properties are calculated at cell faces, and scalar properties are calculated at cell centers, four sets of trilinear interpolation operators are required by three dimensions.

By use of the interpolation functions, we can interpolate the fluid velocity and pressure fields to the particle positions to calculate the fluid/particle drag force and pressure gradient term in Eq. 11. At the same time, we can interpolate the drag force term at the particle positions to the Eulerian grids to calculate the coupling terms in Eq. 2. Besides, the interpolation scheme also enables us to calculate the particle volume fraction for each Eulerian cell by allocating the particle volume to the cell center nodes. One can refer to Snider (2001) for more details about the interpolation issues.

The fluid equations are solved by the Semi-Implicit Method for Pressure Linked Equations algorithm, which is a commonly used algorithm to solve the Navier-Stokes equation. More details about this algorithm can be found in the work of Patankar (2018).

**Propped Fracture Conductivity Calculation.** Propped fracture conductivity is an important parameter controlling the post-fracture productivity. It is a measure of the flow capacity of fluids through a fracture, defined as the product of permeability of the proppant in the fracture and propped fracture width (Economides and Nolte 1989). The proppant transport behaviors during the pumping process can directly affect the propped fracture conductivity.

Many studies have focused on the impact of proppant distribution and its mechanical properties on the propped fracture conductivity, effective fracture geometries, and well performance (Cleary 1980; Cipolla et al. 2009; Warpinski 2009; Neto and Kotousov 2013; Gu and Mohanty 2014; Khanna et al. 2014; Liu et al. 2017; Wang and Elsworth 2018). Most of them assumed proppant distribution as complete settlement and uniform distribution (Warpinski 2009; Neto and Kotousov 2013; Khanna et al. 2014). Only a few considered the heterogeneous proppant distribution in the fracture (Wang and Elsworth 2018). Also, most researchers did not account for the effect of multisize proppant distribution.

Based on the proppant simulation results, our model can accommodate the effect of arbitrary proppant distribution and multisize proppants. In our work, we neglected the effect of proppant embedment and considered proppants as incompressible spheres. Therefore, the most dominant mechanism affecting the propped fracture geometry and propped fracture conductivity is the compaction of the proppant pack after fracturing treatments as the hydraulic pressure releases.

In the proppant simulation, the concentration of the proppant bed varies from location to location. The proppants at the lower region of the proppant bed are close packed, while the upper proppant bed has a relatively loose-packed state. During the slurry injection, the fluidized particles are washed or dragged across the top of the proppant bed. The erosional washing out of the proppant pack from the edges makes loose-packed proppants mobilize from the packed state.

Even though the proppant distribution is nonuniform and heterogeneous within the fracture during pumping, we assume that all the proppants will reach the close-packed state after fracturing treatments because of the effect of compaction **(Fig. 2).** Therefore, once the proppants are compacted, the local proppant concentration will reach the maximum close-packed concentration. The maximum particle volume fraction depends on the shape, size, and ordering of the particles, and it is less than unity because of the existence of void space. In this work, we take 0.65 as our maximum close-packed concentration. Because the initial fracture width is known, we can calculate the propped fracture width based on mass conservation by using Eq. 12.

$$W_i \times \alpha_{pi} = W_{\text{propped}} \times \alpha_{pc}, \quad (12)$$

where $W_i$ is the initial fracture width, m; $W_{\text{propped}}$ is the propped fracture width after compaction, m; $\alpha_{pi}$ is the proppant volume fraction at the end of the pumping; and $\alpha_{pc}$ is the maximum close-packed proppant volume fraction.

Fig. 2—Schematics of the fracture closure process.

After calculating the propped fracture width distribution, the Kozeny-Carman relation (Kozeny 1927; Carman 1937) has been used to calculate the permeability distribution.

$$k = \frac{\phi^3}{CS^2(1-\phi)^2}, \quad (13)$$

where $k$ is the permeability, $\text{m}^2$; $C$ is the Kozeny-Carman constant, which is recommended to be 5 for unconsolidated sandpack (Gu and Mohanty 2014); $\phi$ is the sandpack porosity; $S$ is the particle surface area per unit volume of the solid phase, $\text{m}^{-1}$; and it is closely related to the particle radius $r$, m. For close-packed proppants, smaller proppants tend to have a larger $S$ (Eq. 14).

$$S = \frac{3}{r}. \quad (14)$$

Due to the Lagrangian nature of the MP-PIC method, we can track the motion of every computational parcel, which enables us to locate the distribution of proppants of different sizes. From the proppant size distribution of Lagrangian parcels, we perform the image analysis to extract the information for the proppant distribution of both 40/70- and 100-mesh proppants. After dividing the proppant

distribution into two regions of different proppant sizes, we can apply the Kozeny-Carman relation to calculate the permeability. Once the permeability and propped fracture width are calculated, the propped fracture conductivity can be calculated as

$$kW_{\text{propped}} = 1.1 \times 10^{10} \frac{W_{\text{propped}}}{S^2} \frac{\phi^3}{(1-\phi)^2}, \qquad (15)$$

where both propped fracture width $W_{\text{propped}}$ and particle surface area $S$ are in inches. The fracture conductivity $kW_{\text{propped}}$ has the unit of md-ft. Note that the fracture conductivity calculated by Eq. 15 is the fracture conductivity at initial reservoir pressure. During production, the fracture conductivity will decrease due to the compaction effect of the increasing effective stress.

**Gas Production Simulation.** After calculating the propped fracture width and fracture conductivity, we incorporated them into a reservoir simulation model to predict gas production. Note that, to consider the production from unpropped fractures, we also assigned an unpropped fracture conductivity for all the cases during the production simulation.

As shown in **Fig. 3,** we have built a basic shale gas reservoir model, including a single well and a perfectly symmetrical full fracture. The full fracture was generated from the half fracture in the proppant simulation and conductivity calculation. Through nonneighboring connections, an embedded discrete-fracture modeling formulation was applied to properly model fractures with complex geometries and nonuniform conductivity distribution (Yu 2015; Xu et al. 2017a, 2017b). After calculating the effective wellbore index between fracture and well cells, we ran the reservoir simulation for four cases and performed the visualization of pressure distribution. By comparing the 1,000-day cumulative gas production, we can quantify the impact of different proppant pumping schedules on the well production and give strategies to optimize the field fracturing design.

**Fig. 3—Schematics of the gas production simulation model by incorporating the propped fracture width and fracture conductivity. The reservoir dimension is 200 × 2,065 × 100 ft, which corresponds to reservoir length, width, and thickness, respectively. The fracture is in the middle of the reservoir.**

**Case Study and Results.** Based on the field schedule designs in slickwater fracturing, we have generated four field-scale proppant schedules with a fixed injection rate (10 bbl/min), varying concentration (from 0.5 to 2 ppg), and multisize proppants (40/70 mesh and 100 mesh). The detailed pumping stages are displayed in **Table 1 and Fig. 4,** and the fluid and proppant properties are shown in **Table 2.**

As shown in Fig. 4, the first three proppant schedules (Cases 1, 2, and 3) all have eight stages and 1-hour injection time. During the first four stages, we injected 100-mesh proppants, with concentration gradually increasing from 0.5 to 2 ppg. Starting from the fifth stage, we changed the proppant size from 100 mesh to 40/70 mesh, and the concentration was back to 0.5 ppg. During the next four stages, the slurry concentration gradually recovered to 2 ppg at the end of the pumping. Because both types of proppants have the same density (2650 kg/m$^3$), the only difference between the first three cases is the mass percentage of 100-mesh proppants and 40/70-mesh proppants. We can calculate the mass percentages of proppants based on the detailed stages of each schedule: Case 1—30% of 100-mesh proppants and 70% of 40/70-mesh proppants; Case 2—50% of 100-mesh proppants and 50% of 40/70-mesh proppants; Case 3—70% of 100-mesh proppants and 30% of 40/70-mesh proppants.

Case 4 has the same proppant percentage as Case 2 but with a flush stage after the fracturing treatment. The flush stage consists of less than one wellbore volume of fluid and sweeps the wellbore clean of proppant (Economides and Nolte 1989). Besides cleaning the wellbore, the flush treatment also changes the proppant distribution within the fracture by flushing the proppant pack near the wellbore and forcing the proppant bed to extend deeper into the fracture.

By performing the preceding case studies, in this paper we investigated the impact of proppant pumping schedules on the well production from two perspectives: the mass percentages of 100-mesh and 40/70-mesh proppants, and the flush stage.

| Stage | Proppant Size (Mesh) | Case 1 | | Case 2 | | Case 3 | | Case 4 | |
|---|---|---|---|---|---|---|---|---|---|
| | | Pumping Time (minutes) | Proppant Concentration (ppg) | Pumping Time (minutes) | Proppant Concentration (ppg) | Pumping Time (minutes) | Proppant Concentration (ppg) | Pumping Time (minutes) | Proppant Concentration (ppg) |
| 1 | 100 mesh | 4.5 | 0.5 | 7.5 | 0.5 | 10.5 | 0.5 | 7.5 | 0.5 |
| 2 | | 4.5 | 1 | 7.5 | 1 | 10.5 | 1 | 7.5 | 1 |
| 3 | | 4.5 | 1.5 | 7.5 | 1.5 | 10.5 | 1.5 | 7.5 | 1.5 |
| 4 | | 4.5 | 2 | 7.5 | 2 | 10.5 | 2 | 7.5 | 2 |
| 5 | 40/70 mesh | 10.5 | 0.5 | 7.5 | 0.5 | 4.5 | 0.5 | 7.5 | 0.5 |
| 6 | | 10.5 | 1 | 7.5 | 1 | 4.5 | 1 | 7.5 | 1 |
| 7 | | 10.5 | 1.5 | 7.5 | 1.5 | 4.5 | 1.5 | 7.5 | 1.5 |
| 8 | | 10.5 | 2 | 7.5 | 2 | 4.5 | 2 | 7.5 | 2 |
| 9 | No proppant | – | – | – | – | – | – | 8.5 | 0 |

Table 1—Design of field-scale pumping schedules.

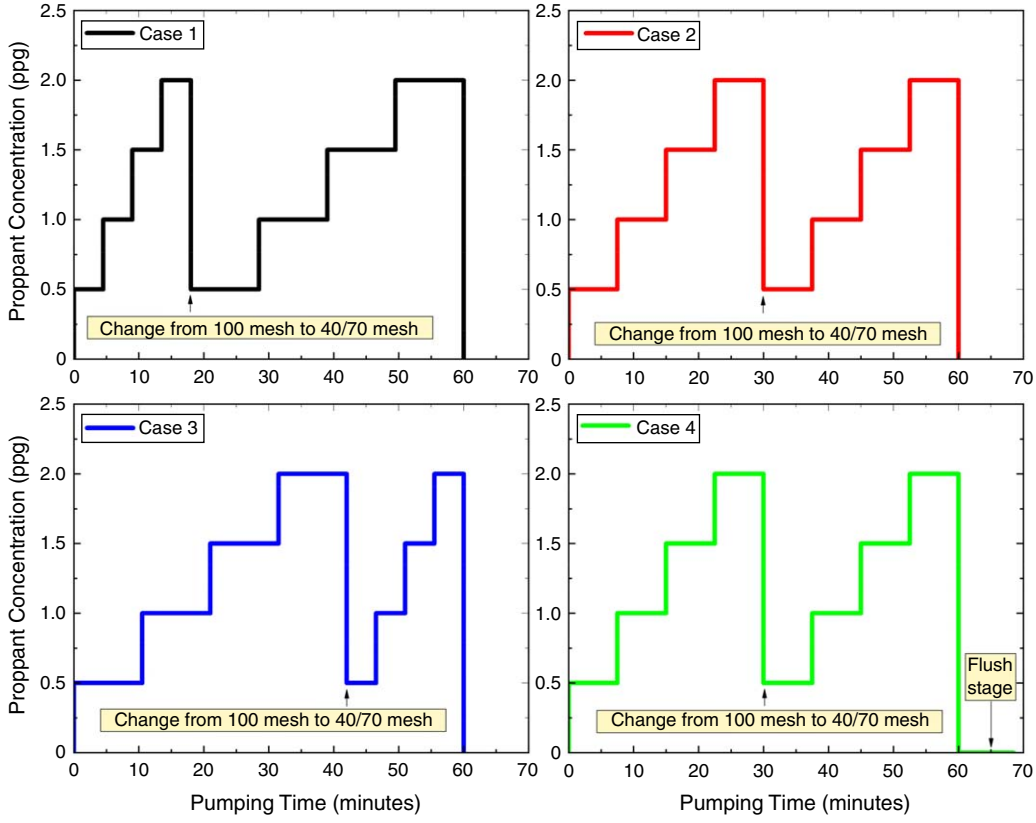


**Fig. 4—Detailed pumping stages for four cases. The first three cases were generated to study the effects of mass percentages of 100-mesh and 40/70-mesh proppants. Case 4 was used to evaluate the effects of a flush stage by comparison with Case 2.**

| Properties | Value | Unit |
|---|---|---|
| Fluid viscosity | 0.01 | Poise |
| Fluid density | 1000 | $kg/m^3$ |
| Proppant density | 2650 | $kg/m^3$ |
| Proppant diameter distribution (40/70 mesh) | Gaussian distribution expectation: $3.2\times10^{-4}$; Variance: $4\times10^{-5}$; Minimum: $2.15\times10^{-4}$; Maximum: $4.25\times10^{-4}$ | m |
| Proppant diameter distribution (100 mesh) | Gaussian distribution expectation: $1.5\times10^{-4}$; Variance: $1\times10^{-5}$; Minimum: $1.25\times10^{-4}$; Maximum: $1.75\times10^{-4}$ | m |

Table 2—Fluid and proppant properties.

**Numerical Model Construction.** As shown in **Fig. 5,** the proppants were injected into a half vertical fracture with a length of 180 m (590.6 ft), a height of 30 m (98.4 ft), and a width of 0.00762 m (0.3 in.). The inlet is on the left side of the fracture, and the outlet is at the right end. In this study, we assumed a predefined static fracture geometry and neglected the effect of fracture propagation and fluid leakoff. We believe these two mechanisms do not have a significant impact on our cases because of the following reasons. In fracturing treatments, the pad stage is injected before the proppant-laden stages, and the fluid moves much faster than the proppants. Therefore, the fractures can be created before the arrival of the proppants so that the effect of fracture propagation on proppant transport is not significant. For the effects of fluid leakoff, except for smaller fracture lengths and widths, one of the most important effects is the screenout phenomenon near the fracture tips. In our cases, all the proppant schedules were generated as stair-stepped, incremental schedules, with a low starting concentration (0.5 ppg). The fluid leakoff therefore can be largely avoided, and its effect on the proppant transport is negligible.

**Proppant Volume Fraction within the Fracture.** For the simulation results, we first calculated the proppant volume fraction (also termed as proppant concentration) distribution within the fracture. As illustrated in **Fig. 6,** all the cases have a severe proppant settling. Once injected into the fracture, most proppants settled to form the proppant bed directly, and the proppant suspension mainly occurred near the injection point. Even though the proppants are packed into the proppant bed, the upper region of the proppant bed can be mobilized by the drag force and the washout effect from the injected slurry. Our proppant simulation can capture the movement of the proppant bed, and these physical mechanisms are well-considered.

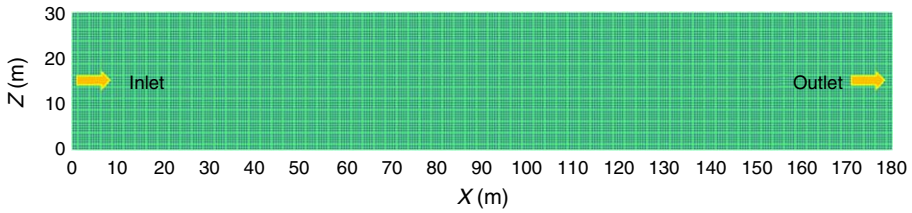


**Fig. 5—Numerical configuration of fracture geometry. The fracture faces have a nonslip boundary condition, and the inlet has a fixed flow-rate boundary condition. The outlet has an outflow boundary condition in which both proppants and fluids can flow out of the fracture.**

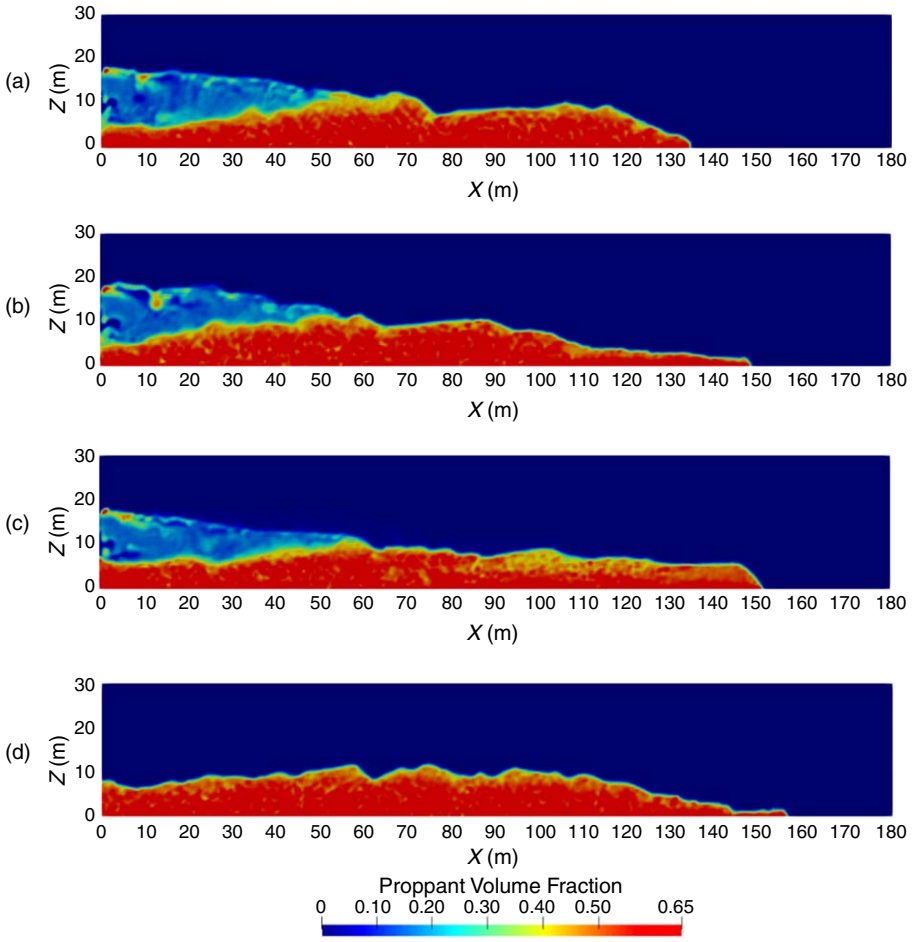


**Fig. 6—Proppant volume fraction distribution within the fracture for four proppant pumping schedules (Cases 1, 2, 3, and 4).**

Because of the severe proppant settling, the propped fracture height is less than half of the hydraulic fracture height. Along the fracture length direction, the proppants can move incredible distances. This simulation result is consistent with the field observation, which has confirmed significant proppant transport distances (over 500 ft for 40/70-mesh proppants) using slickwater (Leonard et al. 2007).

Then we compared the proppant placement of four cases in two aspects: proppant concentration and proppant bed geometry. For the proppant concentration, it is observed that the proppant schedules with a higher percentage of smaller proppants (100 mesh) tend to have a smaller average proppant concentration. From Cases 1 through 3, as the percentage of 100-mesh proppants increases from 30 to 70%, the upper region of the proppant bed area gradually turns to yellow (lower concentration). The reason is that smaller proppants are easier to be suspended by the fluid, while larger proppants (40/70 mesh) tend to settle into the close-packed proppant bed. For Case 4, the flush stage makes almost all the proppants settle into the proppant bed, and the overall proppant concentration is highest among these four cases.

In terms of the proppant bed geometry, we mainly focused on the length and height of the proppant bed. As the percentage of smaller proppants increases, the proppant schedules can have a deeper proppant penetration within the fracture. However, the average proppant bed height decreases a little bit. As illustrated in Fig. 6, from Cases 1 through 3, the proppant transport distance gradually increases, but the average proppant bed height shrinks. The reason is that large proppants have a more severe settling than small proppants so that it is difficult for them to transport a long distance with the fluid. Instead, they will accumulate close to the injection point, forming a high proppant bed. From the standpoint of material balance, if the same amount of proppant is injected, longer proppant transport distance leads to smaller average proppant bed height. Compared with Case 2, the flush stage in Case 4 pushes proppants deeper into the fracture, resulting in a longer proppant transport distance and smaller average proppant bed height.

Benefitting from the Lagrangian nature of the MP-PIC method, we further analyzed the proppant size distribution and proppant age distribution within the fracture. **Figs. 7a through 7d** show the distribution of proppants with two sizes (40/70 mesh and 100 mesh) for four cases, respectively. The blue region represents 100-mesh proppants, and the yellow region means 40/70-mesh proppants. Due to the injection sequence (100 mesh first and 40/70 mesh later), most 100-mesh proppants tend to settle at the bottom of the fracture, and the subsequent 40/70-mesh proppants will accumulate on the top of the 100-mesh proppant bank. The 100-mesh proppants have a longer transport distance than the 40/70-mesh proppants. From Case 1 to Case 3, as we increase the percentage of 100-mesh proppants, the difference between the transport distances of 100-mesh proppants and 40/70 mesh proppants also increases. For Case 1 (30% of 100-mesh proppants), the transport distances of both 100-mesh and 40/70-mesh proppants are almost the same. For Cases 2 (50%) and 3 (70%), the difference between the transport distances increases to 40 m (131.2 ft) and 65 m (213.3 ft), respectively. Note that, instead of a "piston-like" displacement, even though the 100-mesh proppants are easier to go with the fluid, they are not completely displaced by the subsequent 40/70-mesh proppants. There are still some 100-mesh proppants near the wellbore settling at the bottom of the fracture. For Case 4, the flush stage makes both the 100-mesh proppants and 40/70-mesh proppants transport a longer distance in the fracture, especially for the 40/70-mesh proppants.

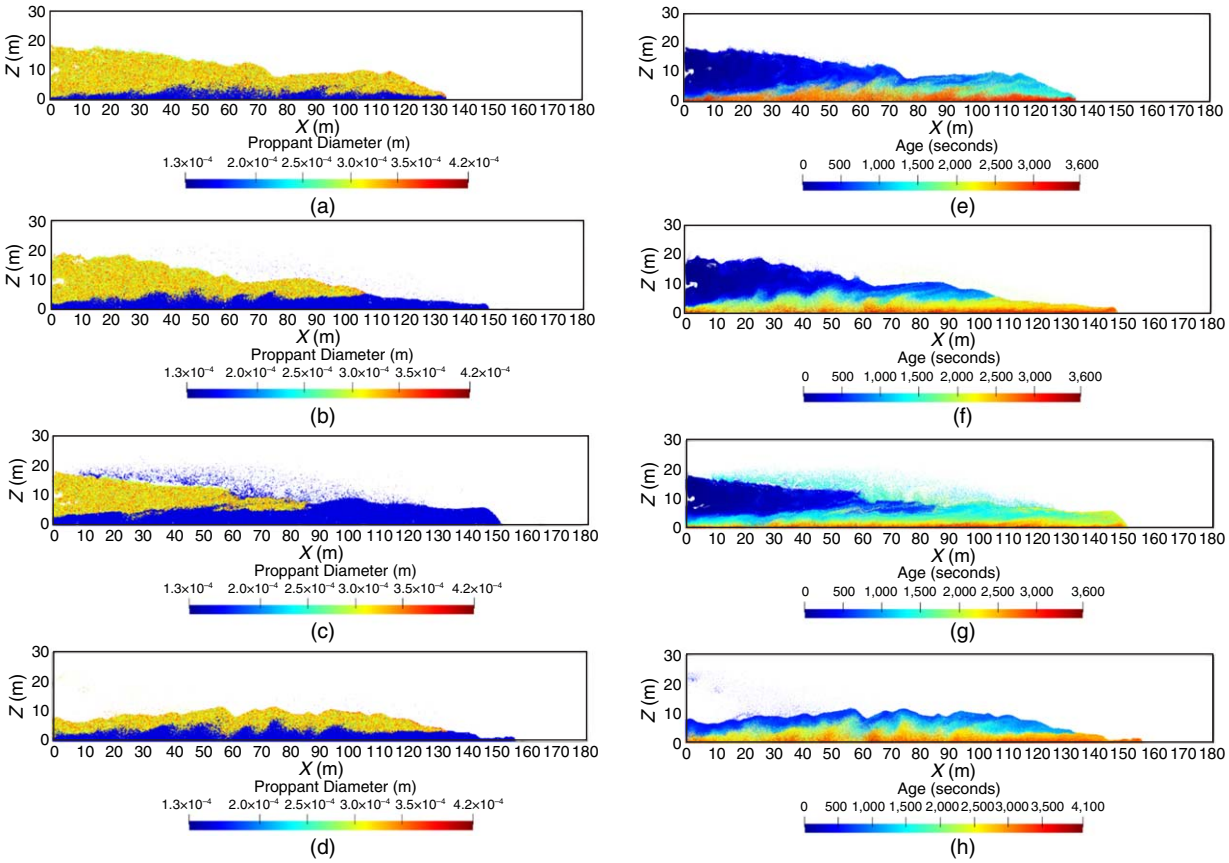


**Fig. 7—(a), (b), (c), and (d) are proppant size distributions within the fracture for four cases, respectively. The blue region represents a small proppant size (100 mesh). The yellow region represents a large proppant size (40/70 mesh); and (e), (f), (g), and (h) are proppant age distribution for four cases, respectively. The blue region means newly injected proppants. The red region means old proppants. The color indicates the residence time of the proppants in the fracture.**

Figs. 7e through 7h are the proppant age plots for four cases, respectively, showing the residence time of the injected proppants in the fracture. It is observed that the proppants injected earlier (red) deposit at the bottom of the fracture, and the proppants injected later (blue) will accumulate on the top of the early proppant bed. For all the pumping schedules, we injected 100-mesh proppants first and 40/70-mesh proppants later. Therefore, the red region represents the 100-mesh proppants, and the blue region represents the 40/70-mesh proppants. By comparing the age plots (Figs. 7e through 7h) and the proppant size distribution (Figs 7a through 7d), we find an excellent agreement. All the preceding analyses provide us with a qualitative understanding of the effects of different pumping schedules on the proppant distribution. To better evaluate these pumping schedules, we applied a propped fracture conductivity model to estimate propped fracture width, permeability, and fracture conductivity for four cases. In this study, the propped fracture width, permeability, and fracture conductivity were calculated based on the proppant simulation results, which did not account for the proppant settling after pumping stops. The reasons why the proppant settling after the shutdown does not have a significant effect on our case study and results are as follows: Slickwater has a poor capability of suspending proppants so that most of the proppants already settled to form the proppant bed during the injection process. The little proppant suspension with a low concentration near the injection point is negligible compared to the large proppant bed; and even though proppants have a long time to settle after the shutdown, they will not form an entirely close-packed proppant bed. The roughness and nonplanarity of the field hydraulic fractures can hinder the proppants from settling. The shrinking fracture widths resulted from the release of fluid pressure can further decrease the proppant settling velocity and suspend the small particles. From the preceding explanation, we believe that the proppant settling after the shutdown will not change the proppant distribution significantly in slickwater fracturing, and its effect on our cases is negligible.

**Distribution of Propped Width, Permeability, and Propped Fracture Conductivity.** As shown in **Fig. 8,** the original fracture width (0.3 in.) shrinks because of the release of the hydraulic pressure after fracturing treatments. The leaving residual aperture is highly heterogeneous within the fracture. One observation from these four cases is that the propped fracture widths are larger at the lower region of the proppant bed. The upper region of the proppant bed, especially the proppant bed edge, has much smaller propped fracture widths. This is because the internal or the lower part of the proppant bed is close packed and has a higher proppant concentration. Even though there is compaction of proppants after fracturing treatments, the fracture can be supported to remain its original width. When it turns to the top edge area of the proppant bed, however, the fracture width shrinks dramatically because of the substantial compaction on the loose-packed proppants.

There are also some differences between these four cases. One is the propped fracture geometry. Similar to our previous discussion, Case 1 has the largest average propped fracture height but the smallest propped fracture length. From Cases 1 through 3, as the percentage of 100-mesh proppants increases, the propped fracture length increases, while the average propped fracture height decreases a little bit. Another difference is the propped fracture width. When we inject a larger percentage of 100-mesh proppants, the fracture has a smaller average propped fracture width. As illustrated in Fig. 8, Case 3 has the largest yellow region area compared with Cases 1 and 2. For Case 4, the flush stage sweeps the proppants deeper into the fracture and makes more proppants turn into the close-packed state. Therefore, it has a larger average propped width after the fracturing treatment compared with Case 2.

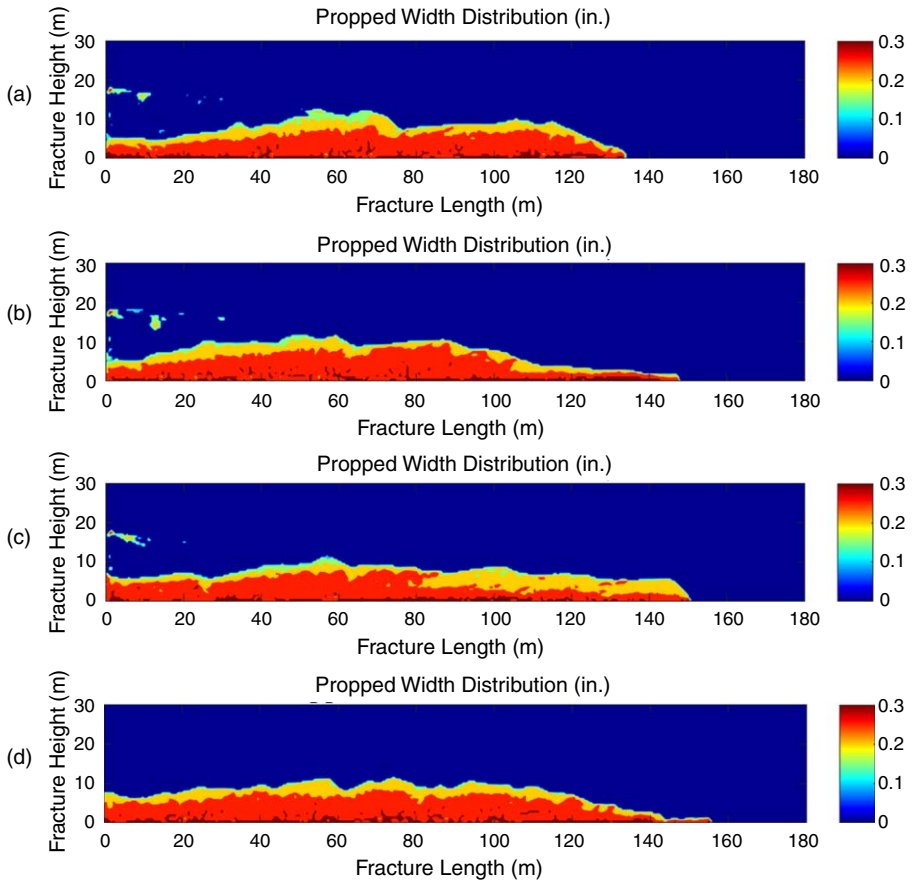


**Fig. 8—Propped fracture width distribution after shutdown for four pumping schedules (Cases 1 through 4).**

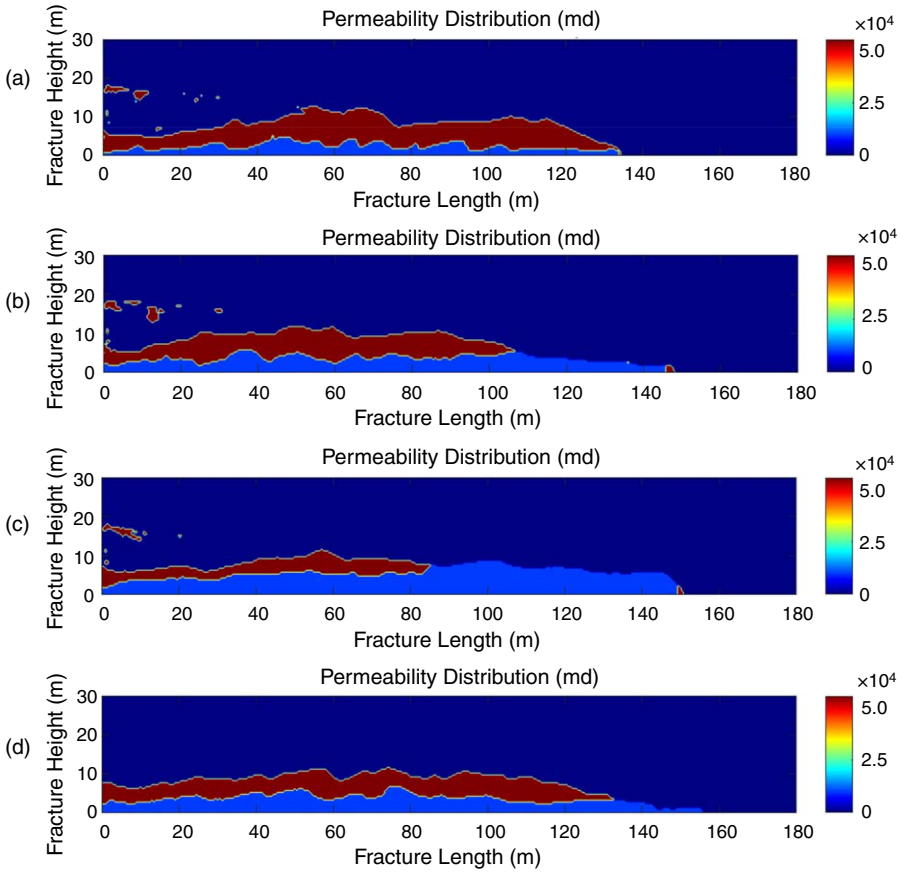


**Fig. 9—Fracture permeability distribution after shutdown for four pumping schedules (Cases 1 through 4).**

After calculating the propped fracture width, we also calculated the permeability distribution for four cases by applying the Kozeny-Carman relation (Eq. 14). As discussed in the methodology part, the permeability is related to the proppant size for close-packed proppants. As shown in **Fig. 9,** for all cases, the permeability distribution is discretized into two regions. The 100-mesh proppants injected earlier settle at the bottom of fracture to form a low-perm proppant bed. The subsequent 40/70-mesh proppants deposited on the top of the100-mesh proppant bed have much higher permeability. Therefore, as the percentage of 100-mesh proppants increases, the high-permeability area decreases. Case 3 has the largest 100-mesh proppants (70%); hence, it has the least high-permeability area. Case 4 has a longer and more uniform high-perm band than Case 2.

By multiplying the propped width and permeability, we calculated the distribution of propped fracture conductivity. As shown in **Fig. 10,** the conductivity distribution differs a lot between cases. Similar to permeability distribution, the conductivity distribution can be divided into the high-conductivity region and the low-conductivity region as well. From Cases 1 through 3, the high-conductivity area gradually decreases as the increase of the percentage of 100-mesh proppants. Case 4 has a longer high-conductivity band compared with Case 2. The changing trend of the high-conductivity area with the increasing percentage of 100-mesh proppants is almost the same as the permeability distribution for four schedules.

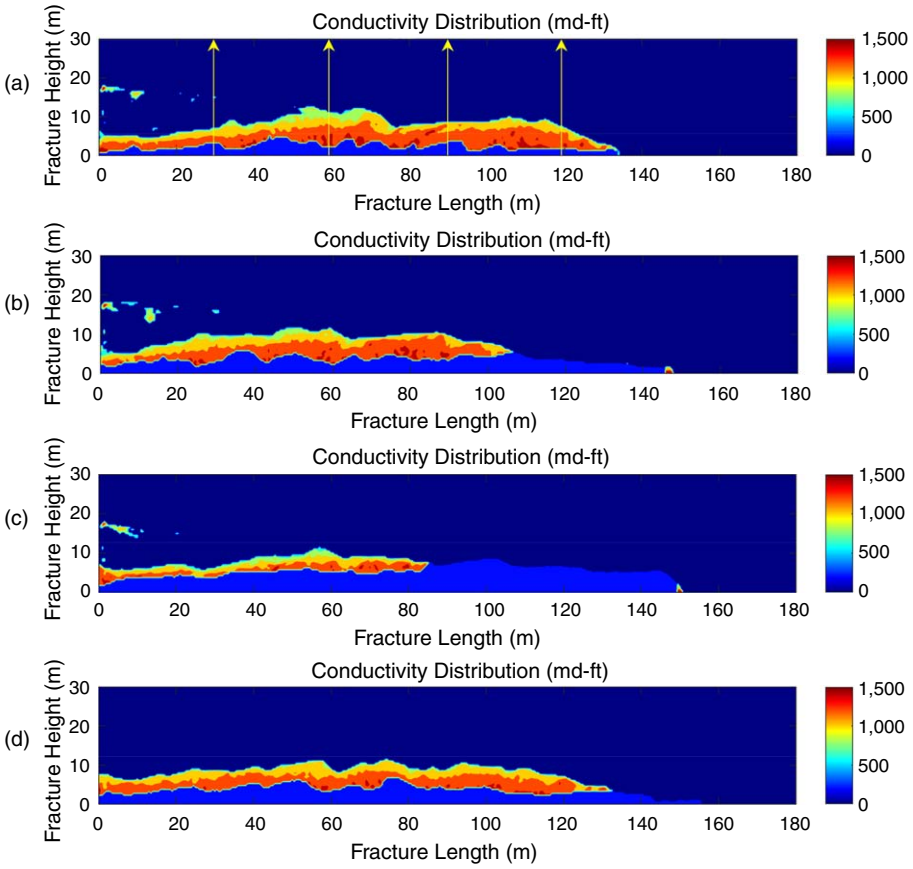


**Fig. 10—Propped fracture conductivity distribution for four pumping schedules (Cases 1 through 4).**

However, unlike the permeability distribution, the fracture conductivity is highly heterogeneous, especially within the high-conductivity region. The fracture conductivity varies a lot in the fracture height direction for all cases. Take Case 1 as an example. We put four vertical lines at the fracture lengths of 30 (98.4), 60 (196.9), 90 (295.3), and 120 m (393.7 ft) to analyze the conductivity along these lines.

As shown in **Fig. 11,** conductivity along four lines show a similar trend with each other. Starting with a small magnitude (750 md-ft), the conductivity has a dramatic increase when we move from the low-conductivity region to the high-conductivity region. However, as we keep moving upward, it declines significantly. When we move to the top edges of the proppant bed or even higher, the conductivity directly drops to zero. The trend indicates that peak conductivity exists in the lower part of the high-conductivity region, which is bordered by the low-conductivity area. This is because the lower part of the high-conductivity region is better propped (larger propped width) by the close-packed proppants compared to the top edges of the proppant bed. As we discussed before, the upper region of the proppant bed can be mobilized by the drag force and the washout effect, and the proppants are loose packed. Therefore, the upper region tends to have a smaller propped fracture width, thus leading to the decaying of the fracture conductivity. However, the lower part of the high-conductivity region has both a large propped width and a high permeability so that it has the highest fracture conductivity.

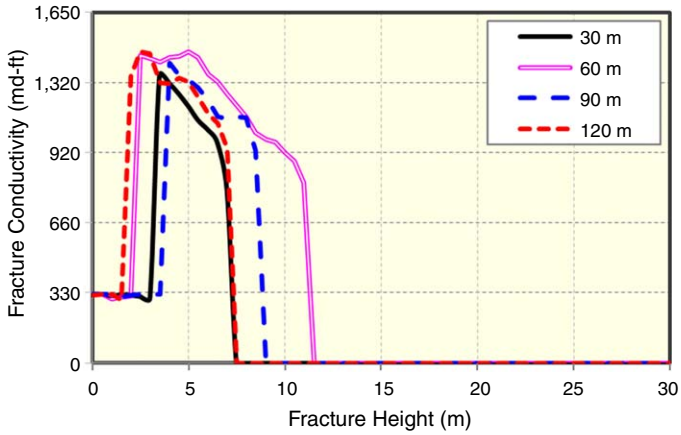


**Fig. 11—Propped fracture conductivity along the fracture height direction at fracture lengths of 30, 60, 90, and 120 m.**

**Comparison of Gas Production Simulation Results.** In this section, we built a shale gas reservoir model, including a single well and a single fracture with complex fracture geometries and nonuniform propped fracture conductivity distribution generated from the preceding proppant simulation results. As shown in **Fig. 12,** to consider the gas production from unpropped fractures, we also assigned an unpropped fracture conductivity to the unpropped fracture area for all the cases. Based on the experimental results (Ghanizadeh et al. 2016; Wu et al. 2017; Wu and Sharma 2019), we set the initial unpropped fracture permeability as 0.5 md, which is four orders of magnitude higher than the matrix permeability and two orders of magnitude lower than the calibrated propped fracture permeability. The residual width for the unpropped fracture was assigned as 0.06 in. For consistency, we assigned the same values of unpropped conductivity for all the four cases.

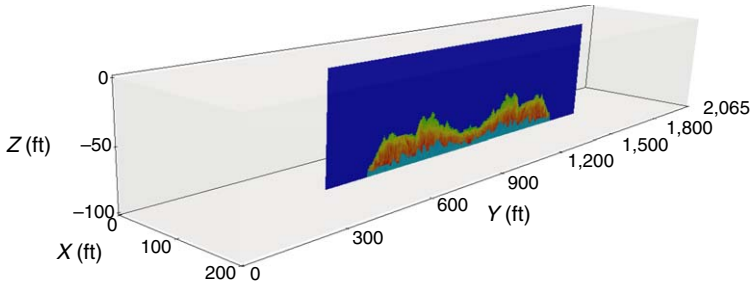

**Fig. 12—Basic shale gas reservoir model including a single well and a single fracture with complex boundaries and nonuniform fracture conductivity distribution.**

In the production simulation, a perfectly symmetric full fracture was generated from the half-fracture results. Note that during production, we assumed that the wellbore is well connected to the near-wellbore region, which means that the wellbore has good communication with the proppant bed. This assumption is acceptable for the following reasons: The near-wellbore region is usually fully fractured and has plenty of fracture branches and networks, which can generate conductive paths and increase the wellbore connectivity; and the high-productivity perforated completions in horizontal wells usually create wedge-shaped perforation channels in the vertical direction, extending from the upper or lower side of the wellbore (Furui et al. 2008), thus significantly improving the communication between the wellbore and the lower proppant bed.

The reservoir model dimension is $200 \times 2065 \times 100$ ft, which corresponds to the reservoir length, width, and thickness, respectively. Single-phase flow of gas with residual water saturation of 10% has been simulated. The other basic reservoir parameters are shown in **Table 3.** Note that Eq. 15 overestimated the propped fracture conductivity without considering the field damage within fractures. In this study, we only used the distribution of calculated propped fracture conductivity and decreased the original propped conductivity by 1,000 times as the input of reservoir simulation. The decreasing ratio can be calibrated by the history match of production data. The range of propped fracture conductivity for reservoir simulation is approximately 0.25 to 1.5 md-ft.

| Parameter | Value | Unit |
|---|---|---|
| Model dimension ($x \times y \times z$) | $200 \times 2{,}065 \times 100$ | ft |
| Initial reservoir pressure | 4,300 | psi |
| Bottomhole pressure | 1,000 | psi |
| Reservoir temperature | 130 | °F |
| Reservoir permeability | 50 | nd |
| Reservoir porosity | 10 | % |
| Residual water saturation | 10 | % |
| Total compressibility | $3 \times 10^{-6}$ | $\text{psi}^{-1}$ |
| Simulation time | 1,000 | days |

Table 3—Basic shale gas reservoir parameters used for production simulation.

During production, the effective stress increases due to the depletion of reservoir pressure, which has a negative impact on the fracture conductivity. In the gas production simulation, a pressure-dependent permeability model (Tripoppoom et al. 2020) has been adopted to account for the effect of stress compaction on the fracture conductivity. The fracture permeability reduction is captured using the permeability modulus $\gamma$, as in Eq. 16.

$$k = k_i \exp[-\gamma(p_i - p)], \quad (16)$$

where $k$ is the pressure-dependent permeability, md; $k_i$ is the permeability at initial reservoir pressure, md; $\gamma$ is the permeability modulus, 1/psi, which is recommended to be 0.07 based on laboratory results (Tripoppoom et al. 2020); $p_i$ is the initial reservoir pressure, psi; and $p$ is the reservoir pressure (psi). The normalized decline rate of the fracture permeability with the decreasing reservoir pressure is shown in **Fig. 13.**

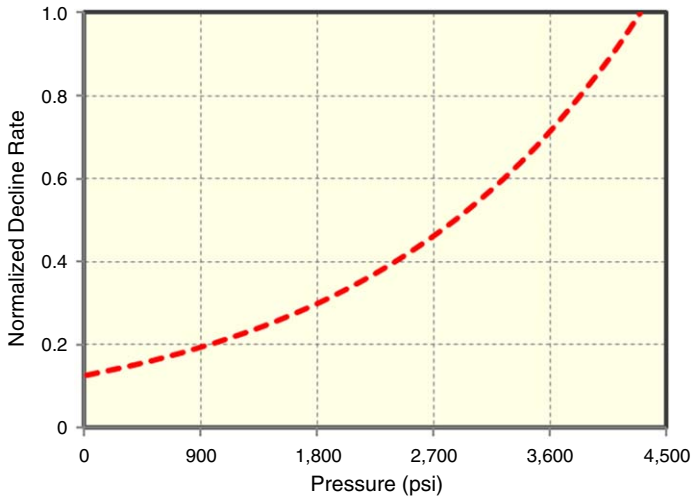


**Fig. 13—Pressure-dependent fracture permeability curve.**

Four cases with different propped fracture geometries and conductivity distribution (at initial reservoir pressure) were simulated and displayed in **Fig. 14.** The propped fracture surface area for each case is approximately 24,146, 24,210, 25,055, and 26,678 $ft^2$, respectively. The nonintrusive embedded discrete-fracture modeling method has been applied for modeling such complex fractures (Xu et al. 2017a, 2017b). Based on the embedded discrete-fracture modeling method, the fracture with complex geometries and nonuniform conductivity distribution can be easily and accurately embedded into the reservoir model without the need of local grid refinement. A constant flowing bottomhole pressure of 1,000 psi was used for a 1,000-day production simulation.

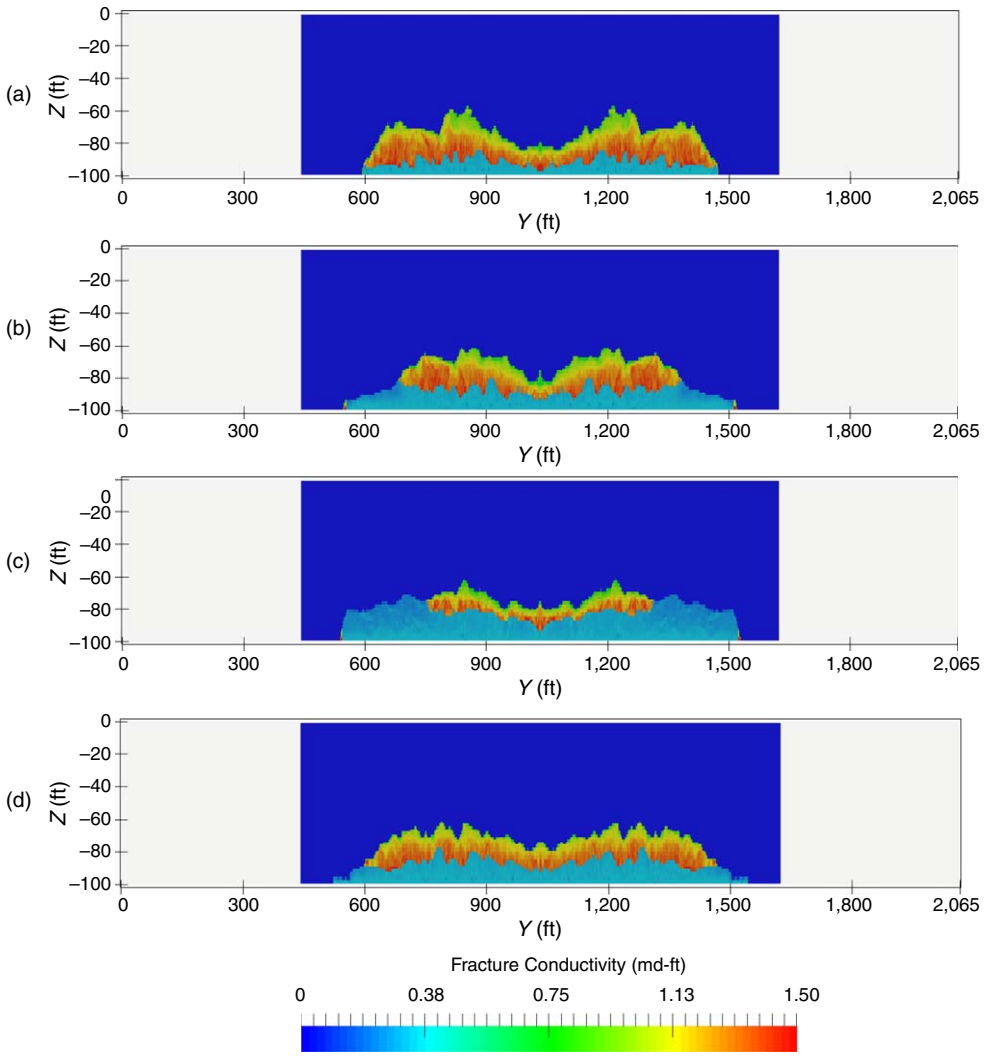


**Fig. 14—Comparison of fracture geometries and conductivity distribution for four cases (Cases 1 through 4).**

**Fig. 15** presents the comparison of the 1,000-day cumulative gas production between four pumping schedules. After 1,000 days, the cumulative gas production of four cases are 23,469, 24,389, 22,034, and 26,396 MMscf, respectively. By comparing the first three cases, we find that Case 2 (50% 100-mesh proppants) has the largest cumulative gas production, which is approximately 10.7% higher than Case 3. As previously discussed, a small percentage of 100-mesh proppants leads to small propped fracture area, and a large percentage of 100-mesh proppants results in a small high-conductivity region.

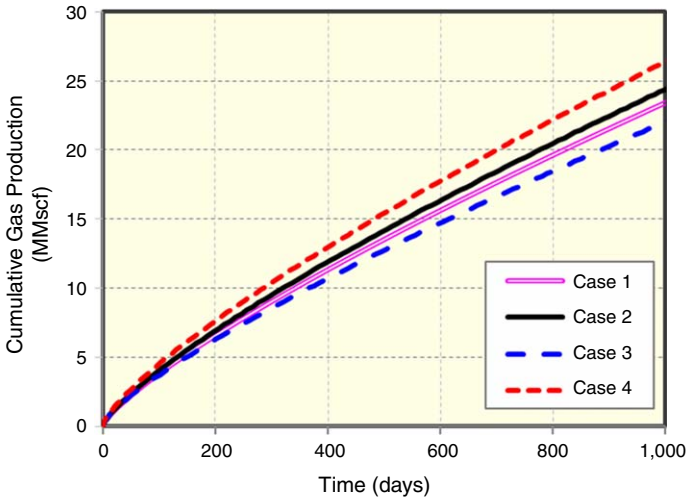


**Fig. 15—Comparison of cumulative gas production in 1,000 days between four cases.**

Among all the cases, Case 4 yields the highest cumulative gas production (19.8% higher than Case 3), and its pressure distribution and drainage volume are shown in **Fig. 16.** Because Cases 4 and 2 have the same percentage of 100-mesh proppants, the only difference is the flush stage. Through the comparison of Cases 4 and 2, we find that the flush stage has improved gas production by approximately 8.2% by forming a longer and more uniform proppant bed. Therefore, the flush stage after slurry injection is well recommended in the field practice.

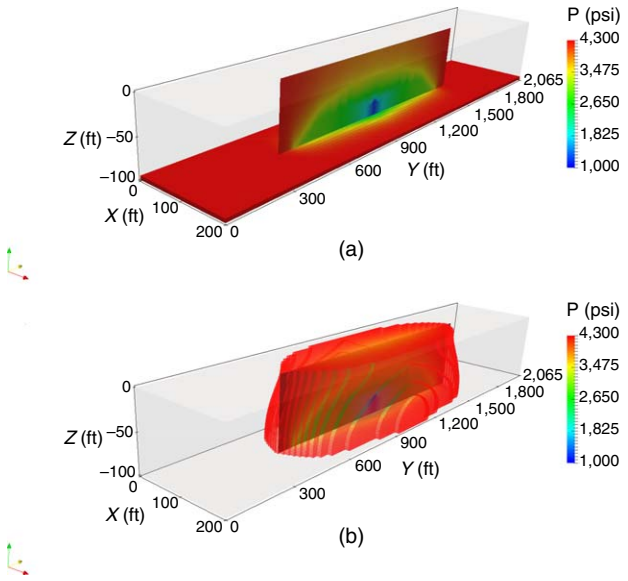


**Fig. 16—(a) Pressure distribution after 1,000 days for Case 4, and (b) drainage volume after 1,000 days for Case 4.**

## Conclusions

In this paper, we have performed an integrated workflow to evaluate the impact of proppant pumping schedules on well production. Combining proppant transport simulation, propped fracture conductivity estimation, and reservoir simulation, this work for the first time presents us with both the qualitative explanation and quantitative evaluation for the impact of proppant pumping schedules at the field scale. We have compared the performance of the pumping schedules with different mass percentages of multisize proppants (100 mesh and 40/70 mesh). Also, we have studied the influence of the flush stage on the final well production. The results of this study give the following conclusions:

1. The MP-PIC method has two advantages: Compared to the E-E methods (e.g., concentration model and two-fluid model), the Lagrangian feature of the MP-PIC method allows us to position every particle so that we can know the exact distribution of different sized proppants. The size distribution enables us to estimate the corresponding permeability for regions of each proppant size; and

compared to the CFD-DEM, the computational parcel feature speeds up the simulation so that we can perform the field-scale proppant simulation.
2. Pumping schedules with the median percentage (50%) of 100-mesh proppants have a better well production than those with small (30%) and large (70%) percentages of 100-mesh proppants. Small percentages of 100-mesh proppants lead to the small propped area. Large percentages result in low conductivity.
3. The flush stage benefits well production. The pure fluid injection after proppant loading can sweep the proppants deeper into the fracture, forming a longer and more uniform proppant bed along the fracture. In our case study, it can improve both the propped area and high-conductivity band, contributing to an 8.2% increase for well production.

## Acknowledgments

This work is supported by the Crisman Institute for Petroleum Engineering Research at Texas A&M University. Prashanth Siddhamshetty and Joseph Sang-II Kwon are grateful for funding support from the National Science Foundation (CBET-1804407) and US Department of Energy (DE-EE000788-10-8, DE-EE000788-9.3). We would also like to thank the High-Performance Research Center (HPRC) at Texas A&M University for providing supercomputer support.

## References

Almulhim, A., Kebert, B., Miskimins, J. et al. 2020. Field-Scale Computational Fluid Dynamics CFD Modeling of Proppant Transport and Distribution within a Horizontal Hydraulic Fracturing Stage. Paper presented at the SPE Hydraulic Fracturing Technology Conference and Exhibition, The Woodlands, Texas, USA, 4–6 February. SPE-199727-MS. https://doi.org/10.2118/199727-MS.

Alotaibi, M. A. and Miskimins, J. L. 2018. Slickwater Proppant Transport in Hydraulic Fractures: New Experimental Findings and Scalable Correlation. *SPE Prod & Oper* **33** (2): 164–178. SPE-174828-PA. https://doi.org/10.2118/174828-PA.

Auzerais, F. M., Jackson, R., and Russel, W. B. 1988. The Resolution of Shocks and the Effects of Compressible Sediments in Transient Settling. *J Fluid Mech* **195** (1): 437–462. https://doi.org/10.1017/S0022112088002472.

Babcock, R. E., Prokop, C. L., and Kehle, R. O. 1967. Distribution of Propping Agent in Vertical Fractures. Paper presented at the Drilling and Production Practice, New York, New York, USA, 1 January. API-67-207.

Boronin, S. A. and Osiptsov, A. A. 2014. Effects of Particle Migration on Suspension Flow in a Hydraulic Fracture. *Fluid Dyn* **49** (2): 208–221. https://doi.org/10.1134/S0015462814020094.

Carman, P. C. 1937. Fluid Flow through Granular Beds. In *Transactions of the AIChE*, Vol. 15, 150–166. New York, New York, USA: AIChE.

Chun, T., Zhang, Z., Mao, S. et al. 2019. Experimental Study of Proppant Transport in Complex Fractures with Horizontal Bedding Planes for Slickwater Fracturing. Paper presented at the SPE/AAPG/SEG Unconventional Resources Technology Conference, Denver, Colorado, USA, 22–24 July. URTEC-2019-547-MS. https://doi.org/10.15530/urtec-2019-547.

Cipolla, C. L., Lolon, E., and Mayerhofer, M. J. et al. 2009. The Effect of Proppant Distribution and Un-Propped Fracture Conductivity on Well Performance in Unconventional Gas Reservoirs. Paper presented at the SPE Hydraulic Fracturing Technology Conference, The Woodlands, Texas, USA, 19–21 January. SPE-119368-MS. https://doi.org/10.2118/119368-MS.

Cleary, M. P. 1980. Analysis of Mechanisms and Procedures for Producing Favorable Shapes of Hydraulic Fractures. Paper presented at the SPE Annual Technical Conference and Exhibition, Dallas, Texas, USA, 21–24 September. SPE-9260-MS. https://doi.org/10.2118/9260-MS.

Crawford, H. R. 1983. Proppant Scheduling and Calculation of Fluid Lost during Fracturing. Paper presented at the SPE Annual Technical Conference and Exhibition, San Francisco, California, USA, 5–8 October. SPE-12064-MS. https://doi.org/10.2118/12064-MS.

Dontsov, E. V. and Peirce, A. P. 2014. A New Technique for Proppant Schedule Design. *Hydraul Fract J* **1** (3).

Dontsov, E. V. and Peirce, A. P. 2015. A Lagrangian Approach to Modelling Proppant Transport with Tip Screen-Out in KGD Hydraulic Fractures. *Rock Mech Rock Eng* **48** (6): 2541–2550. https://doi.org/10.1007/s00603-015-0835-6.

Economides, M. J. and Nolte, K. G. 1989. *Reservoir Stimulation*, Vol. 2. Englewood Cliffs, New Jersey, USA: Prentice Hall.

Furui, K., Zhu, D., and Hill, A. D. 2008. A New Skin-Factor Model for Perforated Horizontal Wells. *SPE Drill & Compl* **23** (3): 205–215. SPE-77363-PA. https://doi.org/10.2118/77363-PA.

Ghanizadeh, A., Clarkson, C. R., Deglint, H. et al. 2016. Unpropped/Propped Fracture Permeability and Proppant Embedment Evaluation: A Rigorous Core-Analysis/Imaging Methodology. Paper presented at the SPE/AAPG/SEG Unconventional Resources Technology Conference, San Antonio, Texas, USA, 1–3 August. URTEC-2459818-MS. https://doi.org/10.15530/URTEC-2016-2459818.

Gu, H. and Desroches, J. 2003. New Pump Schedule Generator for Hydraulic Fracturing Treatment Design. Paper presented at the SPE Latin American and Caribbean Petroleum Engineering Conference, Trinidad and Tobago, 27–30 April. SPE-81152-MS. https://doi.org/10.2118/81152-MS.

Gu, M. and Mohanty, K. K. 2014. Effect of Foam Quality on Effectiveness of Hydraulic Fracturing in Shales. *Int J Rock Mech Min Sci* **70**: 273–285. https://doi.org/10.1016/j.ijrmms.2014.05.013.

Handren, P. J. and Palisch, T. T. 2009. Successful Hybrid Slickwater-Fracture Design Evolution: An East Texas Cotton Valley Taylor Case History. *SPE Prod & Oper* **24** (3): 415–424. SPE-110451-PA. https://doi.org/10.2118/110451-PA.

Harris, S. E. and Crighton, D. G. 1994. Solitons, Solitary Waves, and Voidage Disturbances in Gas-Fluidized Beds. *J Fluid Mech* **266**: 243–276. https://doi.org/10.1017/S0022112094000996.

Hu, X., Wu, K., Song, X. et al. 2018. A New Model for Simulating Particle Transport in a Low-Viscosity Fluid for Fluid-Driven Fracturing. *AIChE J* **64** (9): 3542–3552. https://doi.org/10.1002/aic.16183.

Kern, L. R., Perkins, T. K., and Wyant, R. E. 1959. The Mechanics of Sand Movement in Fracturing. *J Pet Technol* **11** (7): 55–57. SPE-1108-G. https://doi.org/10.2118/1108-G.

Khanna, A., Neto, L. B., and Kotousov, A. 2014. Effect of Residual Opening on the Inflow Performance of a Hydraulic Fracture. *Int J Eng Sci* **74**: 80–90. https://doi.org/10.1016/j.ijengsci.2013.08.012.

Kong, B., Fathi, E., and Ameri, S. 2015. Coupled 3-D Numerical Simulation of Proppant Distribution and Hydraulic Fracturing Performance Optimization in Marcellus Shale Reservoirs. *Int J Coal Geol* **147–148**: 35–45. https://doi.org/10.1016/j.coal.2015.06.006.

Kou, R., Moridis, G. J., and Blasingame, T. A. 2018. Analysis and Modeling of Proppant Transport in Inclined Hydraulic Fractures. Paper presented at the SPE Hydraulic Fracturing Technology Conference and Exhibition, The Woodlands, Texas, USA, 23–25 January. SPE-189856-MS. https://doi.org/10.2118/189856-MS.

Kou, R., Moridis, G., and Blasingame, T. 2019. Bridging Criteria and Distribution Correlation for Proppant Transport in Primary and Secondary Fracture. Paper presented at the SPE Hydraulic Fracturing Technology Conference and Exhibition, The Woodlands, Texas, USA, 5–7 February. SPE-194319-MS. https://doi.org/10.2118/194319-MS.

Kozeny, J. 1927. Uber Kapillare Leitung Der Wasser in Boden. *R Acad Sci Vienna Proc. Cl I* **136**: 271–306.

Leonard, R. S., Woodroof, R. A., Bullard, K. et al. 2007. Barnett Shale Completions: A Method for Assessing New Completion Strategies. Paper presented at the SPE Annual Technical Conference and Exhibition, Anaheim, California, USA, 11–14 November. SPE-110809-MS. https://doi.org/10.2118/110809-MS.

Li, Y., Long, M., Tang, J. et al. 2020. A Hydraulic Fracture Height Mathematical Model Considering the Influence of Plastic Region at Fracture Tip. *Petroleum Exploration and Development* **47** (1): 184–195. https://doi.org/10.1016/S1876-3804(20)60017-9.

Liu, Y. 2006. *Settling and Hydrodynamic Retardation of Proppants in Hydraulic Fractures*. Ph.D. dissertation, University of Texas at Austin, Austin, Texas, USA. http://hdl.handle.net/2152/2766.

Liu, Y., Leung, J. Y., Chalaturnyk, R. et al. 2017. Fracturing Fluid Distribution in Shale Gas Reservoirs due to Fracture Closure, Proppant Distribution and Gravity Segregation. Paper presented at the SPE Unconventional Resources Conference, Calgary, Alberta, Canada, 15–16 February. SPE-185043-MS. https://doi.org/10.2118/185043-MS.

Mao, S., Shang, Z., Chun, S. et al. 2019. An Efficient Three-Dimensional Multi-Phase Particle-in-Cell Model for Proppant Transport in the Field Scale. Paper presented at the SPE/AAPG/SEG Unconventional Resources Technology Conference, Denver, Colorado, USA, 22–24 July. URTEC-2019-462-MS. https://doi.org/10.15530/urtec-2019-462.

Mao, S., Zhang, Z., Chun, T. et al. 2020. Field-Scale Numerical Investigation of Proppant Transport among Multi-Cluster Hydraulic Fractures. *SPE J*. SPE-203834-PA (in press; posted November 2020). https://doi.org/10.2118/203834-PA.

Meng, H. Z. and Brown, K. E. 1987. Coupling of Production Forecasting, Fracture Geometry Requirements and Treatment Scheduling in the Optimum Hydraulic Fracture Design. Paper presented at the SPE/DOE Joint Symposium on Low Permeability Reservoirs, Denver, Colorado, USA, 18–19 May. SPE-16435-MS. https://doi.org/10.2118/16435-MS.

Miskimins, J. L. and Alotaibi, M. 2019. The Impacts of Proppant Sorting and Dune Shape on Slickwater Hydraulic Fracturing Conductivity. Paper presented at the SPE/AAPG/SEG Asia Pacific Unconventional Resources Technology Conference, Brisbane, Australia, 18–19 November. URTEC-198208-MS. https://doi.org/10.15530/AP-URTEC-2019-198208.

Mobbs, A. T. and Hammond, P. S. 2001. Computer Simulations of Proppant Transport in a Hydraulic Fracture. *SPE Prod & Fac* **16** (2): 112–121. SPE-69212-PA. https://doi.org/10.2118/69212-PA.

Neto, L. B. and Kotousov, A. 2013. On the Residual Opening of Hydraulic Fractures. *Int J Fract* **181** (1): 127–137. https://doi.org/10.1007/s10704-013-9828-1.

Nolte, K. G. 1986. Determination of Proppant and Fluid Schedules from Fracturing-Pressure Decline. *SPE Prod Eng* **1** (4): 255–265. SPE-13278-PA. https://doi.org/10.2118/13278-PA.

O'Rourke, P. J. and Snider, D. M. 2010. An Improved Collision Damping Time for MP-PIC Calculations of Dense Particle Flows with Applications to Polydisperse Sedimenting Beds and Colliding Particle Jets. *Chem Eng Sci* **65** (22): 6014–6028. https://doi.org/10.1016/j.ces.2010.08.032.

Palisch, T. T., Vincent, M., and Handren, P. J. 2010. Slickwater Fracturing: Food for Thought. *SPE Prod & Oper* **25** (3): 327–344. SPE-115766-PA. https://doi.org/10.2118/115766-PA.

Patankar, N. A. and Joseph, D. D. 2001. Lagrangian Numerical Simulation of Particulate Flows. *Int J Multiphase Flow* **27** (10): 1685–1706. https://doi.org/10.1016/S0301-9322(01)00025-8.

Patankar, S. 2018. *Numerical Heat Transfer and Fluid Flow*. Oxfordshire, England, UK: Taylor & Francis.

Roostaei, M., Nouri, A., Fattahpour, V. et al. 2018. Numerical Simulation of Proppant Transport in Hydraulic Fractures. *J Pet Sci Eng* **163**: 119–138. https://doi.org/10.1016/j.petrol.2017.11.044.

Schein, G. 2005. The Application and Technology of Slickwater Fracturing. Paper SPE-108807-DL presented as a Distinguished Lecture during the 2004–2005 season.

Sharma, M. M. and Gadde, P. B. 2005. The Impact of Proppant Retardation on Propped Fracture Lengths. Paper presented at the SPE Annual Technical Conference and Exhibition, Dallas, Texas, USA, 9–12 October. SPE-97106-MS. https://doi.org/10.2118/97106-MS.

Siddhamshetty, P., Wu, K., and Kwon, J. S. I. 2018. Optimization of Simultaneously Propagating Multiple Fractures in Hydraulic Fracturing to Achieve Uniform Growth Using Data-Based Model Reduction. *Chem Eng Res Des* **136**: 675–686. https://doi.org/10.1016/j.cherd.2018.06.015.

Siddhamshetty, P., Wu, K., and Kwon, J. S. I. 2019. Modeling and Control of Proppant Distribution of Multistage Hydraulic Fracturing in Horizontal Shale Wells. *Ind Eng Chem Res* **58** (8): 3159–3169. https://doi.org/10.1021/acs.iecr.8b05654.

Snider, D. M. 2001. An Incompressible Three-Dimensional Multi-Phase Particle-in-Cell Model for Dense Particle Flows. *J Comput Phys* **170** (2): 523–549. https://doi.org/10.1006/jcph.2001.6747.

Tang, J., Wu, K., Li, Y. et al. 2018. Numerical Investigation of the Interactions between Hydraulic Fracture and Bedding Planes with Non-Orthogonal Approach Angle. *Eng Fract Mech* **200**: 1–16. https://doi.org/10.1016/j.engfracmech.2018.07.010.

Tang, J., Wu, K., Zuo, L. et al. 2019. Investigation of Rupture and Slip Mechanisms of Hydraulic Fractures in Multiple-Layered Formations. *SPE J*. **24** (5): 2292–2307. SPE-197054-PA. https://doi.org/10.2118/197054-PA.

Tripoppoom, S., Xie, J., Yong, R. et al. 2020. Investigation of Different Production Performances in Shale Gas Wells Using Assisted History Matching: Hydraulic Fractures and Reservoir Characterization from Production Data. *Fuel* **267**: 117097. https://doi.org/10.1016/j.fuel.2020.117097.

Tong, S. and Mohanty, K. K. 2016. Proppant Transport Study in Fractures with Intersections. *Fuel* **181**: 463–477. https://doi.org/10.1016/j.fuel.2016.04.144.

Tsai, K., Fonseca, E., Lake, E. et al. 2013. Advanced Computational Modeling of Proppant Settling in Water Fractures for Shale Gas Production. *SPE J*. **18** (1): 50–56. SPE-151607-PA. https://doi.org/10.2118/151607-PA.

Wang, J. and Elsworth, D. 2018. Role of Proppant Distribution on the Evolution of Hydraulic Fracture Conductivity. *J Pet Sci Eng* **166**: 249–262. https://doi.org/10.1016/j.petrol.2018.03.040.

Warpinski, N. R. 2009. Stress Amplification and Arch Dimensions in Proppant Beds Deposited by Waterfracs. Paper presented at the SPE Hydraulic Fracturing Technology Conference, The Woodlands, Texas, USA, 19–21 January. SPE-119350-PA. https://doi.org/10.2118/119350-PA.

Wen, C. Y., and Yu, Y. H.1966. Mechanics of Fluidization. In *Chemical Engineering Progress Symposium Series* **62** (62): 100–111.

Wu, C.-H. and Sharma, M. M. 2019. Modeling Proppant Transport through Perforations in a Horizontal Wellbore. *SPE J*. **24** (4): 1777–1789. SPE-179117-PA. https://doi.org/10.2118/179117-PA.

Wu, W., Kakkar, P., Zhou, J. et al. 2017. An Experimental Investigation of the Conductivity of Unpropped Fractures in Shales. Paper presented at the SPE Hydraulic Fracturing Technology Conference and Exhibition, The Woodlands, Texas, USA, 24–26 January. SPE-184858-MS. https://doi.org/10.2118/184858-MS.

Xu, Y., Cavalcante Filho, J. S. A., Yu, W. et al. 2017a. Discrete-Fracture Modeling of Complex Hydraulic-Fracture Geometries in Reservoir Simulators. *SPE Res Eval & Eng* **20** (2): 403–422. SPE-183647-PA. https://doi.org/10.2118/183647-PA.

Xu, Y., Yu, W., and Sepehrnoori, K. 2017b. Modeling Dynamic Behaviors of Complex Fractures in Conventional Reservoir Simulators. Paper presented at the SPE/AAPG/SEG Unconventional Resources Technology Conference, Austin, Texas, USA, 24–26 July. URTEC-2670513-PA. https://doi.org/10.15530/URTEC-2017-2670513.

Yi, S. S., Wu, C.-H., and Sharma, M. M. 2018. Proppant Distribution among Multiple Perforation Clusters in Plug-and-Perforate Stages. *SPE Prod & Oper* **33** (4): 654–665. SPE-184861-PA. https://doi.org/10.2118/184861-PA.

Yu, W. 2015. *Developments in Modeling and Optimization of Production in Unconventional Oil and Gas Reservoirs*. Ph.D. dissertation, University of Texas at Austin, Austin, Texas, USA. http://hdl.handle.net/2152/31623.

Zeng, J., Li, H., and Zhang, D. 2016. Numerical Simulation of Proppant Transport in Hydraulic Fracture with the Upscaling CFD-DEM Method. *J Nat Gas Sci Eng* **33**: 264–277. https://doi.org/10.1016/j.jngse.2016.05.030.

Zeng, J., Li, H., and Zhang, D. 2019. Numerical Simulation of Proppant Transport in Propagating Fractures with the Multi-Phase Particle-in-Cell Method. *Fuel* **245**: 316–335. https://doi.org/10.1016/j.fuel.2019.02.056.

Zhang, M., Prodanović, M., Mirabolghasemi, M. et al. 2019. 3D Microscale Flow Simulation of Shear-Thinning Fluids in a Rough Fracture. *Transp Porous Media* **128**: 243–269. https://doi.org/10.1007/s11242-019-01243-9.

Zhang, Z., Mao, S., Shang, Z. et al. 2020. Numerical Study of Proppant Transport in Field-Scale Fractures for Slickwater Fracturing. Paper prepared for presentation at the 54th US Rock Mechanics/Geomechanics Symposium, physical event cancelled, 28 June–1 July. ARMA-20-1170.